Blind areas in frequency swept reflectometry: Identification, full wave phenomena, shape impact and reconstruction techniques

R. B. Morales[1], S. Hacquin[2,3], S. Heuraux[1], and R. Sabot[2]

[1] *IJL, University of Lorraine, UMR 7198 CNRS, 54506 Vandoeuvre, France*
[2] *IRFM, CEA Cadarache, 13108 Saint-Paul-lez-Durance, France*
[3] *EUROfusion Programme Management Unit, Culham Science Centre, Culham, OX14 3DB, United Kingdom*

1 Motivation

During a discharge in fusion experiments, many phenomena can introduce perturbations in the density profile. The small scale turbulence fluctuations generate an overall change in the acquired phase signal and the inversion process of the fluctuation properties is investigated via a transfer function, as initially approached in [1] and more recent developments are found in [2]. For isolated perturbations, the signature in the reflectometer signal is related to the size of the perturbation. The spectrum of the phase signal can be used to describe the perturbation shape in some small scale cases (in the order of the probing wavelength), as presented in [3]. Here, on the other hand, bigger perturbations, out of the Born approximation validity, are investigated, focusing on perturbations that introduce a valley in the density profile that is large enough such that the probing microwaves have no reflection inside the valley. Such perturbations can occur during massive gas injections, pellet injections, MHD activity or in magnetic islands. If the reconstruction method does not incorporate identification and reconstruction tools for these blind regions, big discrepancies can appear in the reconstructed profile. An example is shown in Fig. 1 using the WKB phase as the input signal and the standard Bottollier-Curtet algorithm [4] with a fixed integration weight factor W equals to 2/3 (assuming a square root refractive index shape inside the integration step) [5]. It is clear that the standard reconstruction does not describe well the perturbation. Furthermore, if the oscillations are smoothed, the perturbation would be neglected entirely.

Even though the probing microwaves have no reflections inside the blind region, there is information to be explored from the higher frequencies that propagate through the perturbation. The parameters necessary to describe a perturbation are: the perturbation width; the perturbation depth; and the perturbation shape. For simplicity, the first perturbations investigated have a well known shape and width and are inserted in a region with linear f_R profile. The idea is to reconstruct the density profile using the unperturbed signal, and afterwards, use the perturbation signature to estimate its properties. To determine the perturbation depth, a signature in the time-of-flight signal is scaled to the perturbation depth (for each given width and shape). As a proof of concept, this procedure is developed in the next section for signals simulated using the WKB approximation to compute the phase evolution. Afterwards, the reflectometer signal is simulated with a 1D full-wave wave equation solver to take into account full-wave effects such as tunnelling, wave-trapping, interference and scattering. Then, the influence of the perturbation shape on the perturbation signature is observed, and lastly, the reconstruction techniques are discussed.

2 Proof of concept in WKB framework

In this section, a proof of concept is done using the time-of-flight signal simulated under the WKB approximation. The simplest method to reconstruct the perturbation is to relate the perturbation

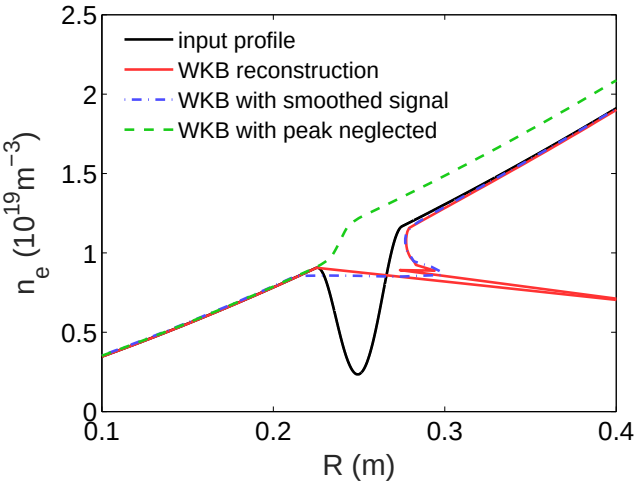

Figure 1: Reconstruction of a density profile containing a blind region and applying the standard Bottollier-Curtet algorithm with $W = 2/3$.

depth to the height of the spike in the time-of-flight signal. In Fig. 1, an example density profile containing a valley is reconstructed. If no change is implemented in the usual Bottollier-Curtet algorithm In Fig. 2, it is shown a time-of-flight signal computed under the WKB approximation for the profile presented in Fig. 1.

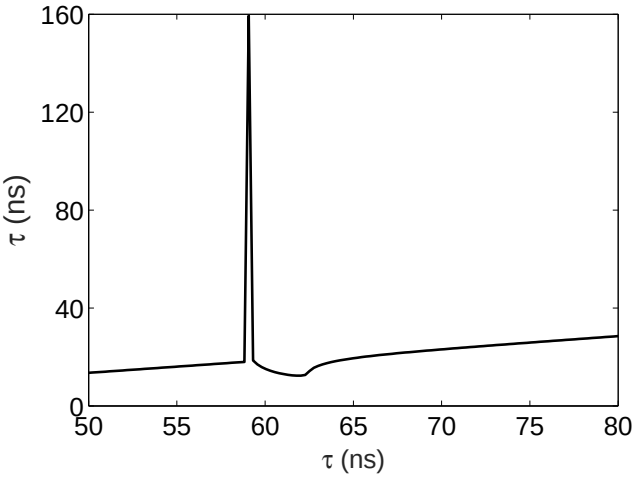

Figure 2: Time of flight during a frequency sweep, computed under the WKB approximation for the example density profile of Fig. 1.

The height of the peak present in the phase evolution signal can be related to the perturbation depth. In Fig. 3, it is illustrated the obtained relation when introducing Gaussian perturbations with a known fixed width, radial position and background magnetic field in typical ranges of fusion plasma parameters.

Using this relation, one can reconstruct a perturbation profile that is inside of the boundary condition assumed. Applying this procedure to the example case of Fig. 1 results in the reconstructed profile in Fig. 4.

The procedure described above can successfully reconstruct the density profile of blind regions under the assumed conditions. However, the experimental signals are more complex than the WKB

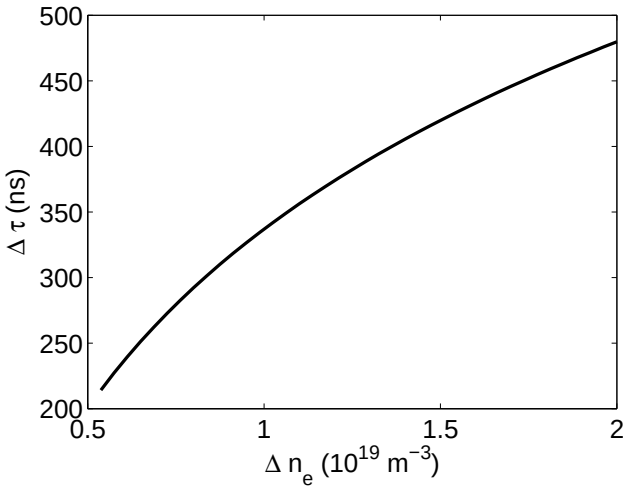

Figure 3: Relation of the phase jump to the depth of a Gaussian perturbation with a fixed width, position and background magnetic field.

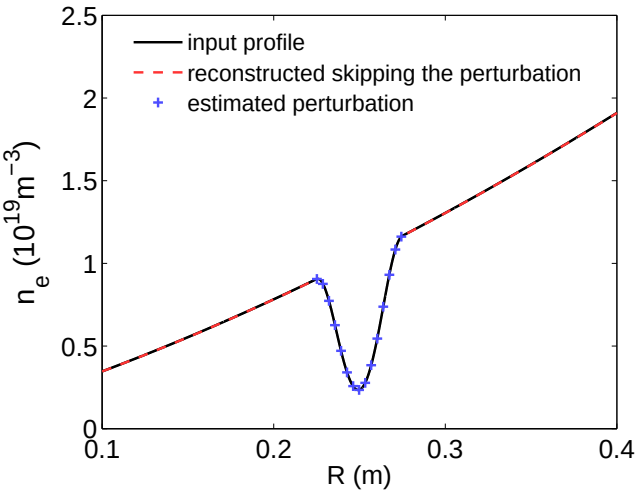

Figure 4: When using the relation in Fig. 3 to describe a Gaussian perturbation of a fixed width.

solution. In the next sections, a full-wave, 1D wave equation solver code is used to simulate the phase-shift signals. Not only the WKB solution is out of its domain of validity in some parts, but in addition, time-dependant full-wave phenomena are present in the full-wave simulated signals.

3 Introduction to full-wave effects in the simulated signals

In order to investigate the full-wave effects from blind regions, the perturbations are introduced in a linear cut-off frequency (f_R) profile. Since the phase evolution depends not only on the density but also on the magnetic field, working in the f_R framework allows to account for both the density and the magnetic field together. Certainly the phase evolution also depends on the f_{pe} to f_{ce} ratio, but this ratio will not vary significantly in the core plasma. This effect will be investigated later when specifically investigating these perturbations in edge conditions.

In this section, perturbations with a sine squared shape are subtracted from the f_R profile. The sine squared shape was chosen for its characteristics of having null magnitude and derivative each

half wavelength. This allows for smooth local implementation on top of the assumed profile. An example of such a perturbation is presented in Fig. 5, with 6.4 cm width and varying depth. The respective time-of-flight signals are presented in Fig. 6. The extraction of the reflectometer time of flight signal is implemented equivalent to the experimental IQ detection technique, as elaborated in [6].

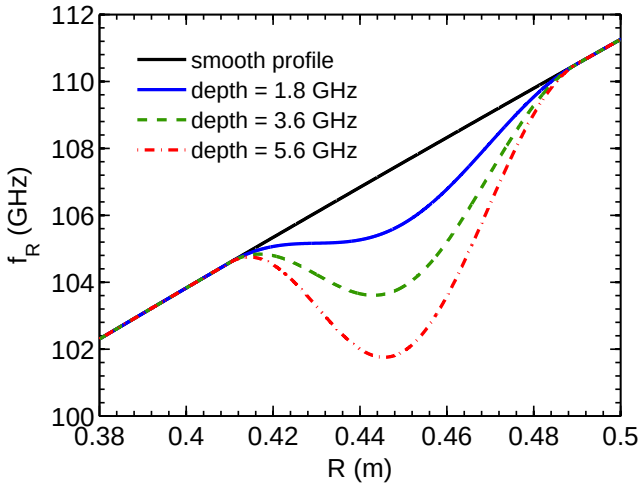

Figure 5: Linear f_R profiles with sine square shaped valleys of different depths.

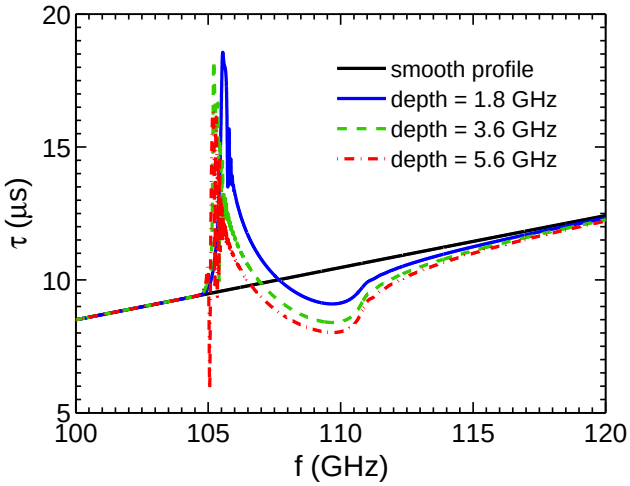

Figure 6: Time-of-flight signals from the profiles introduced in Fig. 5, calculated with the IQ method. The sweeping rate used was 20 GHz/μs as standardized in the latest generation of reflectometers in use.

As can be seen in Fig. 6, the height of the peak in time-of-flight is no longer a good scaling parameter to the perturbation depth, as done in the previous section for the WKB computed phase. The reason is because of the big fluctuations in vicinity of the peak. Other features along the higher frequencies are explored to extract information from the perturbation size. But first, all different signatures of different effects are discussed in order to clarify all features in the full-wave signals.

The fluctuations over the time-of-flight jump are due to frequency mixing caused by the time-dependent effects around the perturbation. As the probing frequency is swept and arrives at the jump frequency, there will be a small band of frequencies that will partially tunnel into the

perturbation. The tunnelling effect is further explored in Sec. 4. In the most complicated scenarios, the tunnelling plus the valley can act as a system of three partially reflecting mirrors. Between the three mirror system, a given frequency can be trapped for some time and return later in the reflected signal. The frequency mixing also occurs if the plasma is probed just above the perturbation frequency. The probing wave propagates much slower through the perturbation, but at a slightly higher frequency, the group velocity through the perturbation is much higher. These two effects can cause a probing frequency close to the jump to arrive later in the signal than a higher frequency. In addition, the cavities between these interfaces can fulfil a resonance condition. In this case a spike is seen in the time-of-flight signal at the resonant frequency. Some resonance cases are observed in Sec. 5. The reflection coefficient of each interface in such three mirror system can be computed from the refractive index jump, according to Ref. [7]. Steep jumps in refractive index can also lead to strong Bragg backscattering for the frequencies above the perturbation. This effect is demonstrated analytically in Ref. [8], and can be observed in Sec. 6 for a square perturbation.

The new full-wave features in the time-of-flight signal, as discussed above, are discussed in Secs. 4, 5 and 6, followed by an analysis on the perturbation shape. The influence on the time-of-flight signal from the perturbation skewness and kurtosis is discussed in Secs. 7.1 and 7.2, respectively. As can be seen in 6, the size of the jump in the time of flight signal is not anymore a good scaling feature of the perturbation signature because this area is very prone to interferences. Instead, the inversion methods will need to extract the information from higher frequencies. An example method is proposed to estimate the size of these $sine^2$ perturbations in Sec. 8 using the integral of the perturbation signal, and some elements of the generalization of the perturbation shape are discussed in Sec. 9.

4 Amplitude drop and tunnelling effect

An additional information from the full-wave signal is the receiving wave amplitude extracted using the IQ detection method, as seen in Fig. 7 for the cases in Fig. 5.

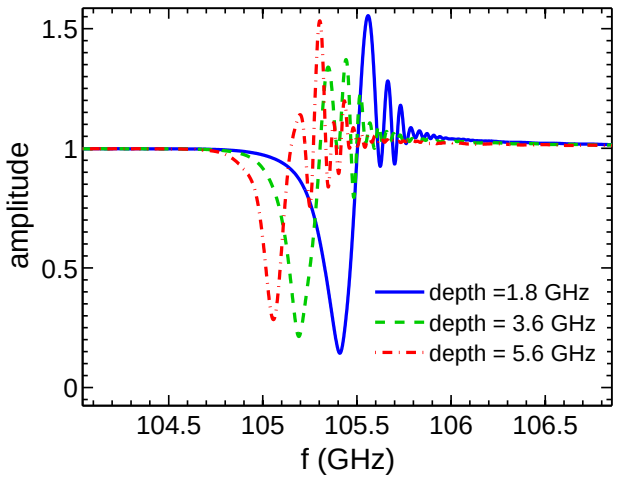

Figure 7: Amplitude from the profiles introduced in Fig. 5 with valleys of 8 cm width, calculated with the IQ method.

The drop in the amplitude signals can be used as a tool to identify the presence of a blind region. It must be coupled to the expected jump in the time-of-flight. The amplitude changes are due to the electromagnetic flux conservation and the frequency mixing effect. As the probing frequency approaches the jump frequency, the microwaves start to partially tunnel into the perturbation and the IQ amplitude signal starts to decrease. The frequencies that partially tunnelled into the perturbation eventually return to the antenna later on. This is why the amplitude drop is followed

by an amplitude increase. As these delayed waves return to the antenna, they interfere with higher probing frequencies, which explains the modulations after the amplitude dip.

The frequency at which this interference starts and ends will depend on the quality factor of the cavities (inside the tunnelling region or inside the perturbation). An example of an early start of interference is given in Fig. 8, where the barrier before the valley is around 1 cm, the interference starts as soon as the amplitude starts decreasing and has a higher oscillation frequency. In this last case, the occurrence of Bragg backscattering leads to the observed modulations. It occurs because the spectrum of the assumed perturbation contains wave-numbers fulfilling the Bragg rule.

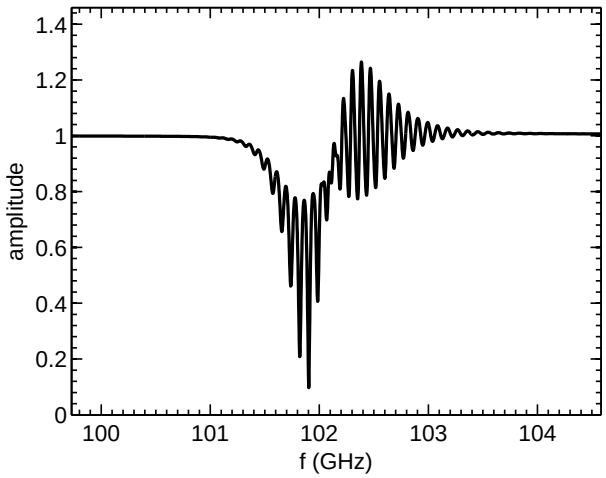

Figure 8: Amplitude from IQ detection for the tunnelling of a shorter tunnelling barrier of 1 cm width.

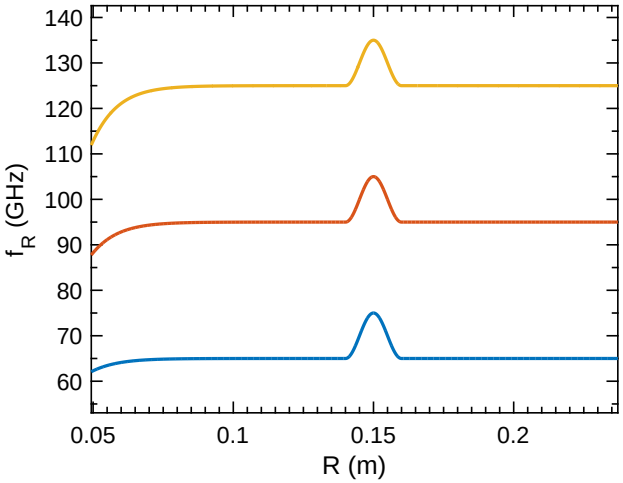

Figure 9: Perturbations for tunnelling studies at varying probing frequencies.

The time at which the tunnelled waves return is impossible to be well determined experimentally. The frequency at which the microwaves start tunnelling, on the other hand, are related to the probing frequency and the barrier width. For the tunnelled waves to be reflected back, they must have an evanescent path equal or longer than the width of the barrier to cross into the perturbation. The analytical expression for the fields of the evanescent wave is demonstrated in Ref. [7]. In practice, the tunnelling band is explored in this section for varying probing frequencies

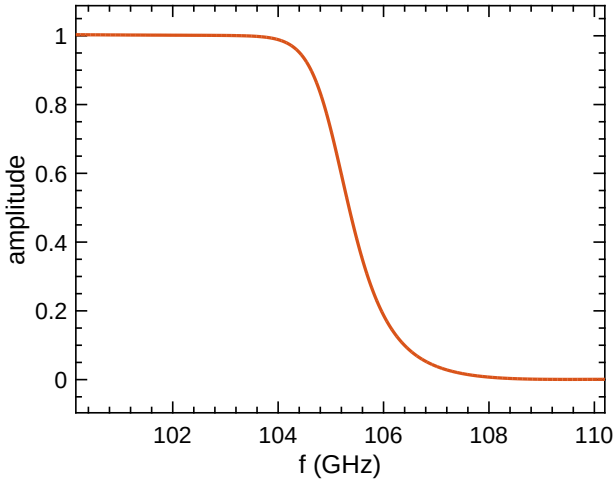

Figure 10: Drop in amplitude from sweeping through a perturbation until no signal is detected.

and perturbation width. The simulations performed involved having a sine square bump on top of a plateau, as depicted in Fig. 9. After going through the top of the perturbation, the waves are damped in the end of the grid on a perfectly matching layer. The respective simulated amplitude for the middle perturbation is given in Fig. 10.

Because in this condition no waves return after they go through the perturbation, the amplitude signals decrease until being zero. The rate of the amplitude drop is related to the probing frequency and the perturbation width. One way to measure the drop rate is to relate the half amplitude drop to the frequency band necessary to achieve it. Doing this for varying widths and probing frequencies lead the the relations in Fig. 11.

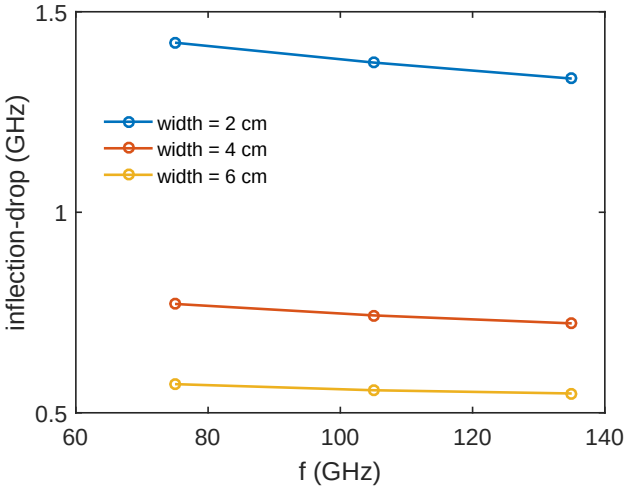

Figure 11: The drop in amplitude observed for varying peak widths and probing frequencies.

Fig. 11 shows that there is little dependency on the probing frequency, compared to the dependency on the perturbation width. Regardless of the presence of interferences, the initial frequency where the amplitude starts to decrease marks the start of the tunnelling effect. By knowing the injected frequency, and therefore the value of f_R, the radial evanescent wave amplitude can be computed, according to [7], by:

$$A_{ev} = A_0 e^{-k\chi r}, \tag{1}$$

with A_{ev} being the evanescent wave amplitude, A_0 is the impinging wave amplitude, k is the impinging wave wave-number, and χ is the imaginary part of the refractive index.

By having the local plasma parameters to compute χ, the path length of the evanescent wave can be computed, i.e. the thickness of the barrier on that probing frequency.

5 Resonances

If one cavity on the three mirror system has a high quality factor and resonate with the injected frequencies, a resonance appears on the time of flight signal. Fig. 12 shows a positive and a negative spike due to a resonance, each peak at its own resonance. The response is sensitive to the frequency sweeping rate because the quality factor of the cavity influences the build up and relaxation of the trapped waves.

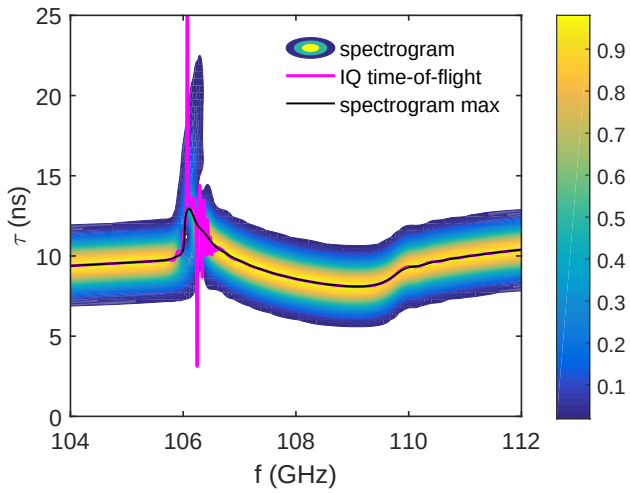

Figure 12: IQ spectrogram and instantaneous frequency signals with a positive and a negative resonance.

For usual resonances on smooth perturbations, the injected waves are not trapped for a long time. This is observed on Fig. 12 because the spectrogram signal does not show any long lasting frequency after the peak in the time of flight. The resonance peak is apparent in the instantaneous frequency signal but seems to not disturb significantly the spectrogram signal. The modulation and resonances are very hard to identify in experimental data because of the innate noise level in experimental signals. Thus, the inversion technique is more robust if using a bigger bandwidth with the frequencies above the time of flight jump. In addition, the maximum of the spectrogram is the signal less sensitive to these modulations.

In the next section, a square perturbation is introduced in the f_R profile to enhance the Bragg backscattering and the reflections in the three mirror system.

6 Reflections and Bragg backscattering from square perturbations

As introduced in Sec. 4, the Bragg backscattering and the reflections in the perturbation three mirror systems are enhanced for a sharper and larger refractive index change. In order to illustrate a case with strong wave trapping, resonance conditions and Bragg backscattering, a square perturbation shape is introduced in the f_R profile as in Fig. 13.

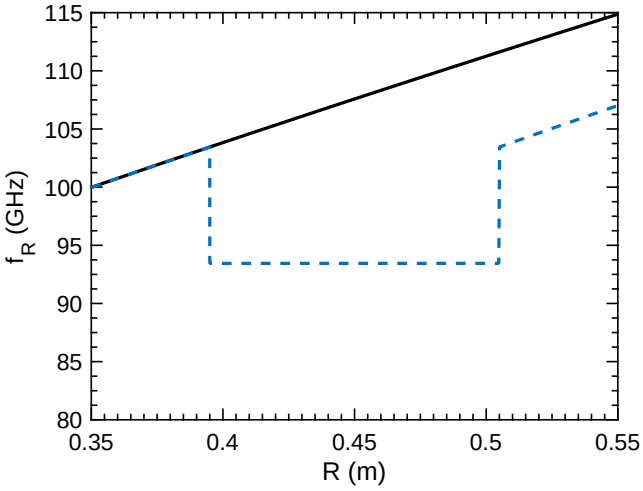

Figure 13: Square perturbation to investigate the uniformity of the time-of-flight contribution across the perturbation.

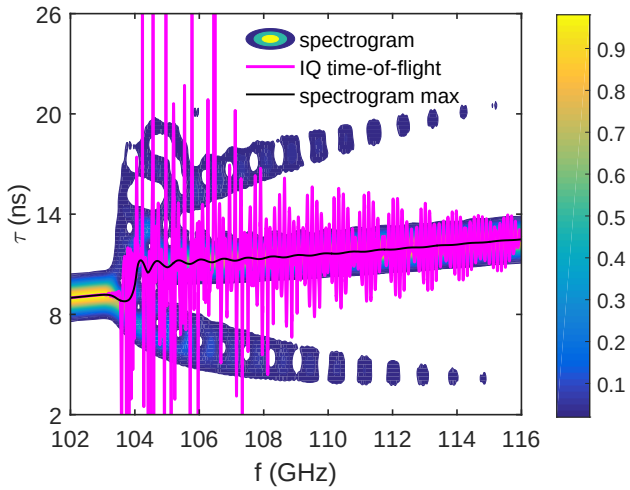

Figure 14: IQ spectrogram and instantaneous frequency signals for the square perturbation on Fig. 13.

The IQ spectrogram and instantaneous frequency signals are presented in Fig. 14. The instantaneous frequency signal shows many resonant frequencies and modulations. After the time-of-flight jump, two additional branches arise in the spectrogram. The upper branch belongs to waves that were trapped and arrive later in the antenna, and the lower branch belongs to reflections that occurred before the cut-off reflection, i.e. the Bragg backscattering component. The spectrogram maximum signal is still smooth and continuous but contain small fluctuations. In order to remove these effects from the main reflection in the cut-off, one can use tomography techniques to apply a narrow band filter that follows the beat frequency evolution, as introduced in [9]. The different frequency components being trapped inside the perturbation can also be observed if plotting the spectrogram of the electric field on a fixed position inside the perturbation, as in Fig. 15. In this case it is more evident to see which are the trapped frequencies and how fast they exit the perturbation. A small frequency band around the first frequency going into the perturbation is very well trapped and end up never fully exiting the perturbation during this short simulation. The tunnelling of the lower frequencies are also visible, although less intense, and are trapped for a short

period. The elongation of a higher frequency, around half GHz above the strongly trapped band, shows a resonance, although trapped only shortly. The resonance condition in this case seems to be roughly +/- 0.5 GHz around the strongly trapped band. Although a square perturbation is not very realistic, additional echoes are seen quite often experimentally and this analysis can be extended to these cases.

The square perturbation is analysed again in the next section when investigating the shape influence on the time-of-flight jump.

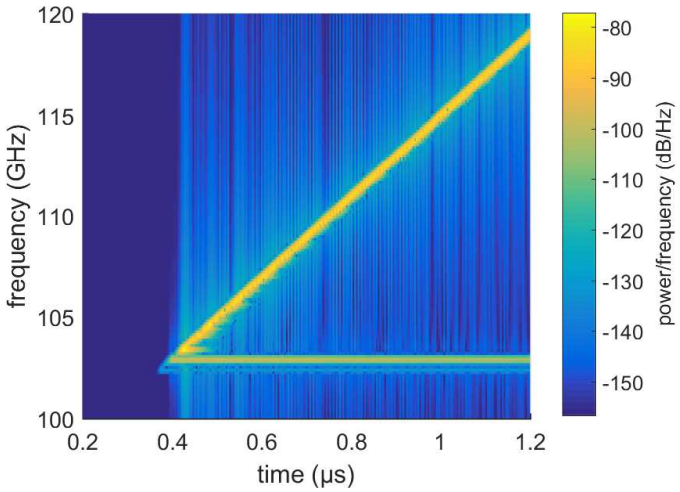

Figure 15: Spectrogram of the electric field inside the square perturbation from Fig. 13.

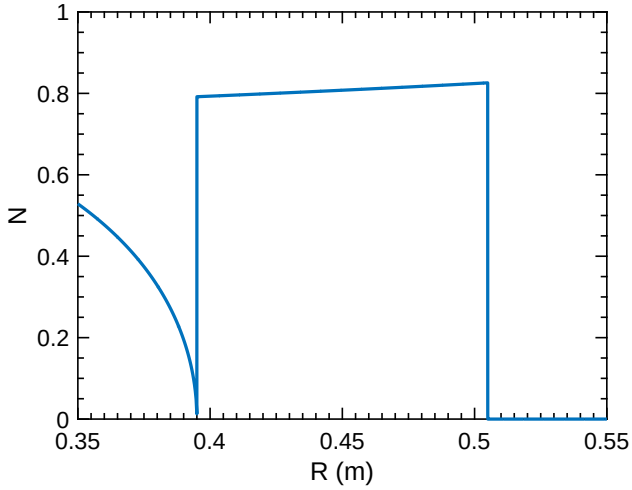

Figure 16: Refractive index over a uniform square perturbation, as introduced in Fig. 13 for a probing frequency just above the time of flight jump.

7 Influence of the perturbation shape on the time-of-flight signal

This section explores the influence of the perturbation shape on the perturbation signature in the time-of-flight signal. The two shape aspects investigated are the perturbation skewness and the

perturbation kurtosis. These effects are treated separately in the next two subsections.

7.1 Effect from the perturbation skewness.

The skewness of a perturbation can be understood as the perturbation radial symmetry. The phenomenon was firstly observed by using skewed triangular shapes and noting how the time-of-flight evolved through the perturbation. To illustrate the effect of the radial non-uniform contribution to the time-of-flight signal, the symmetrical square perturbation of Fig. 13 is investigated. The resulting refractive index inside this perturbation can be observed in Fig. 16 for a probing frequency just above the time of flight jump.

The radially non-uniform refractive index distribution inside the perturbation, as seen in Fig. 16, is caused by the radially non-uniform ratio of f_{pe} to f_{ce}. Although this effect is visible, it is a second order effect and will be neglected in the perturbation reconstruction techniques in the plasma core, since this ratio will not vary much. This effect will be revisited when investigating blind regions in very low densities at the plasma edge.

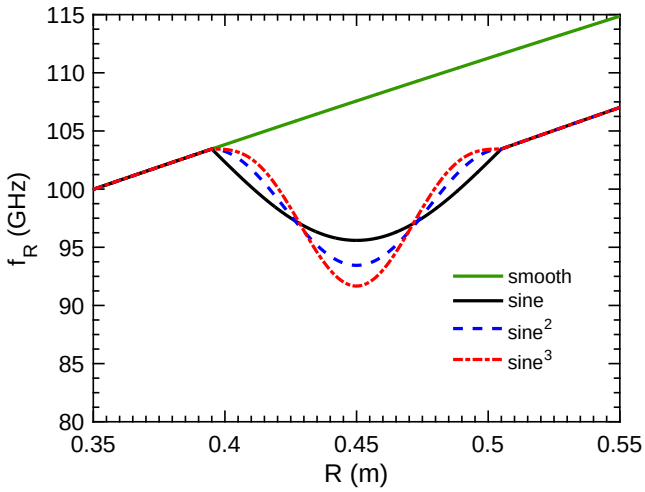

Figure 17: Perturbations with varying kurtosis over a linear f_R profile.

7.2 Effect from the perturbation kurtosis.

The kurtosis of the perturbation is an indication if the perturbation is more concentrated in the center or in the extremities. To investigate this effect, three shapes of perturbation are introduced in the f_R profile, as depicted in Fig. 17.

The three shapes chosen have the same area in the f_R profile. Since the time-of-flight signature is related to the refractive index area over the perturbation, this effect can be seen in the refractive index profile across these perturbations, as given in Fig. 18 for a probing frequency just above the time of flight jump. They are related to the time-of flight signature because the area of the refractive index gives the phase and the time-of-flight is the derivative of the phase.

Fig. 17 shows how the different perturbations have decreasing area in the refractive index profile as the kurtosis is increased (the perturbation becomes more elongated). The best way to make clear which radial positions contribute more to the time-of-flight signature, is to compute the profile of the differential time-of-flight when probing with a frequency slightly above the perturbation. The result is illustrated in Fig. 19. The total time-of-flight after crossing the perturbation is given by the area under the differential time-of-flight, as it is represented in the legend of the figure.

Fig. 19 shows how the perturbations cause a larger time-of-flight contribution the higher is the f_R in the borders of the perturbation, or equivalently, the more they are elongated if keeping a constant area. This happens because the probing waves propagate much slower when propagating

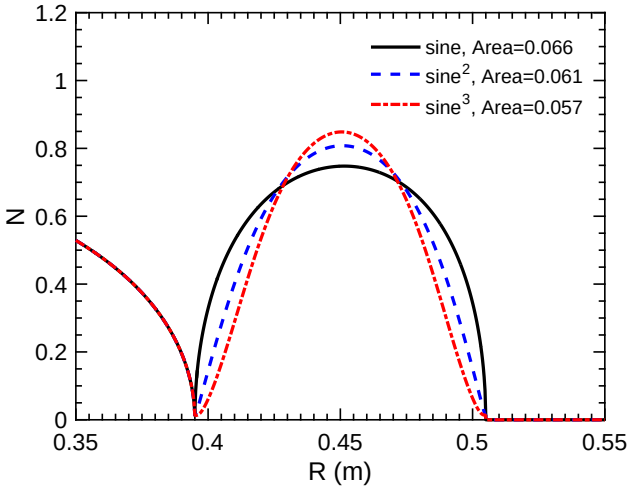

Figure 18: The refractive index profile inside the perturbations with varying kurtosis from Fig. 17, probed just above the time of flight jump.

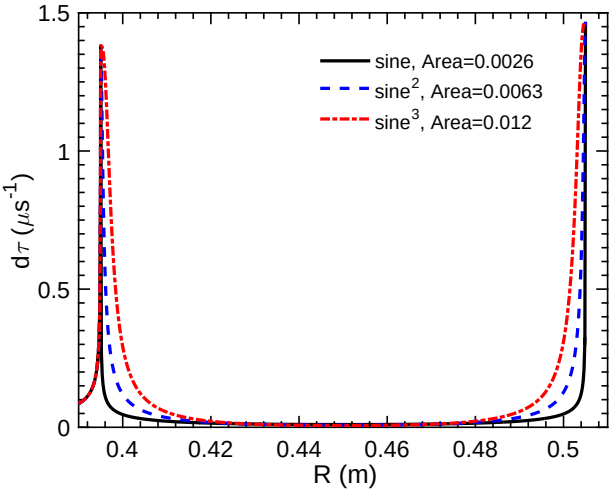

Figure 19: Differential time-of-flight when probing with a frequency slightly above the perturbations of Fig. 17. The legend gives the time-of-flight integrated over the perturbation.

through a region with f_R close to the probing frequency. This means that the bottom of the perturbation have a much lower contribution to the time-of-flight jump compared to the edges.

This effect raises another question. If the bottom of a valley perturbation has less impact on the time-of-flight, it means that the deeper the valley is, the less visible the signature of a given δf_R will be. This accuracy can be inferred by analysing perturbations with different depth, and comparing the time-of-flight after the perturbation, with and without an additional δf_R of constant area. The profiles simulated for this case are displayed in Fig. 20.

Computing the differential time-of-flight when probing at a frequency slightly above the perturbation gives the results in Fig. 21.

Fig. 21 shows that the deeper is the perturbation, the less visible the contribution from the δf_R becomes. To determine exactly how much is this difference, Fig. 22 shows the time-of-flight difference between the profile with and without the δf_R, at the three different depths studied. The δf_R introduced causes an observable contribution in the time-of-flight when the valley is a few GHz deep. However, its contribution on a valley 10 GHz deep is quite small. In an experimental signal

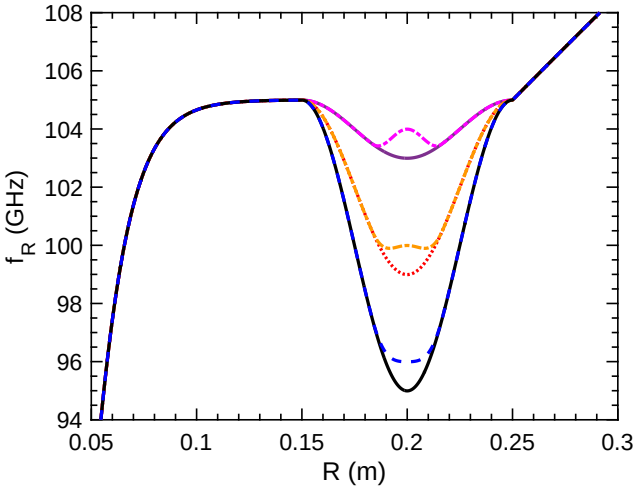

Figure 20: Profiles with perturbations of varying depths, with and without an additional δf_R of constant area. The plateau before the perturbation is introduced to decrease the frequency bandwidth tunnelled into the perturbation. Doing so reduces the interferences, and therefore, reduces the fluctuations on the time-of-flight signal.

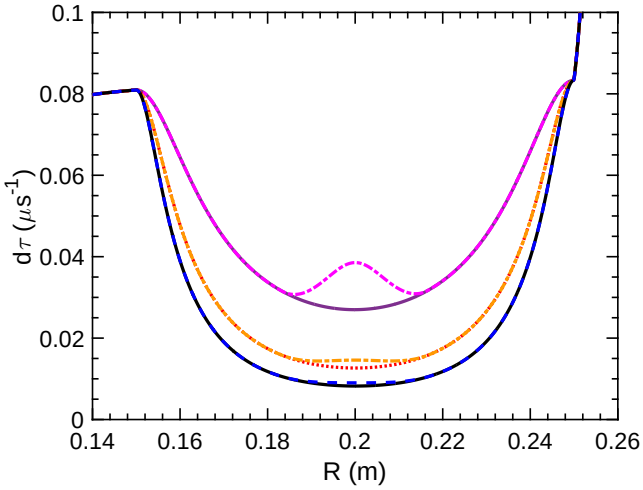

Figure 21: Differential time-of-flight for the profiles in Fig. 20 when probing slightly above the perturbation frequency.

with background noise, such small structures inside deep valleys are indiscernible.

8 Methods to estimate the perturbation size

The first step to estimate the perturbation profile is to detect that a perturbation exists. This can be done from the drop in amplitude coupled to the jump in the time-of-flight signal. The start point of the perturbation is still possible to be conventionally determined, and the end point is either directly after the jump, or it is marked with the bottom of a valley in the time-of-flight signal in the case that the perturbation ends shortly after the jump in time-of-flight. The parameters left to be determine are the perturbation depth and shape. The shape is assumed known in this first instance and in the future, the full wave effects will be explored to extract information about the

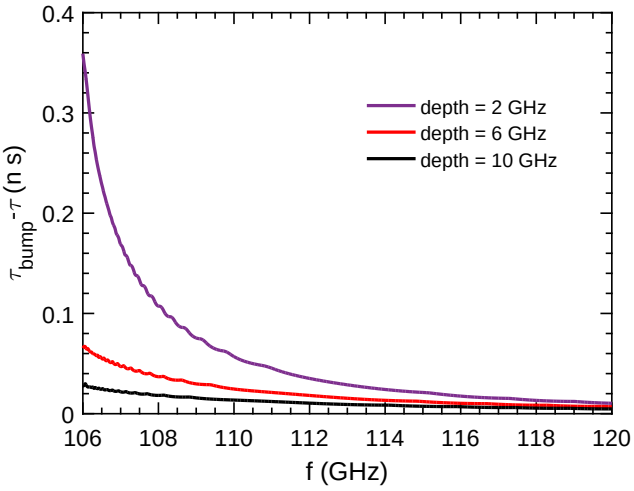

Figure 22: Time-of-flight difference between valleys without and with a positive δf_R perturbation, as introduced in Fig. 20. The probing frequency range starts just after the jump in time-of-flight.

perturbation shape. The depth can be scaled to the perturbation signature similarly to the WKB approach in Sec. 2. However, as it was demonstrated, the amplitude of the jump in time-of-flight is not a consistent scaling parameter anymore, because of the tunnelling, frequency mixing and resonance effects. However, these effects appear in a narrow band around the time-of-flight jump. Between 0.5 and 1 GHz before and after the time-of-flight jump, depending on the conditions, the signal is again compatible with the WKB approximation and have other intuitive scaling features. One example taken from Fig. 6 is the integral of the time-of-flight taken from the point after the jump where it crosses the unperturbed signal, until it converges back to the unperturbed signal. An example of the signal left to be analysed is displayed in Fig. 23.

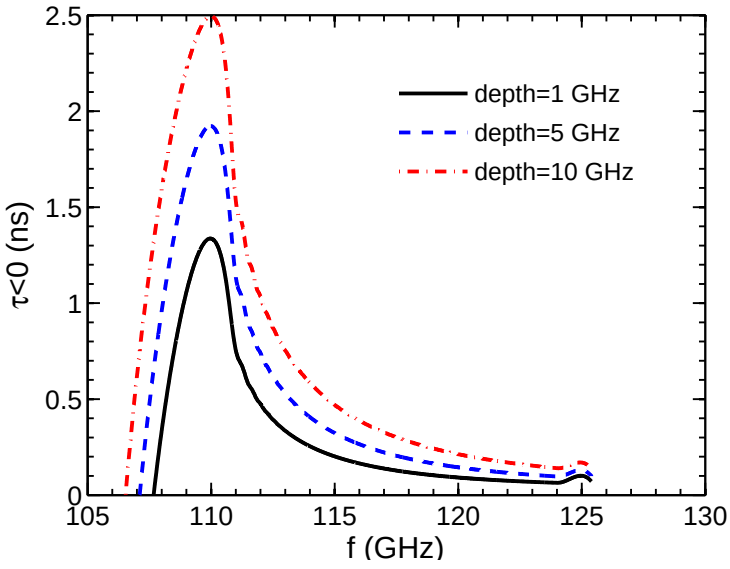

Figure 23: Drop in time-of-flight from $sine^2$ perturbations as introduced in Fig. 6, if subtracted by the smooth solution, starting when the signals with perturbation crosses the unperturbed solution.

From Fig. 23, it is evident that the bigger the perturbation, the bigger is the integral of these signals until it converges back to the unperturbed case. For each fixed width, scanning the

perturbation depth and computing the integral of the signals as displayed in Fig. 23 results in the relations present in Fig. 24.

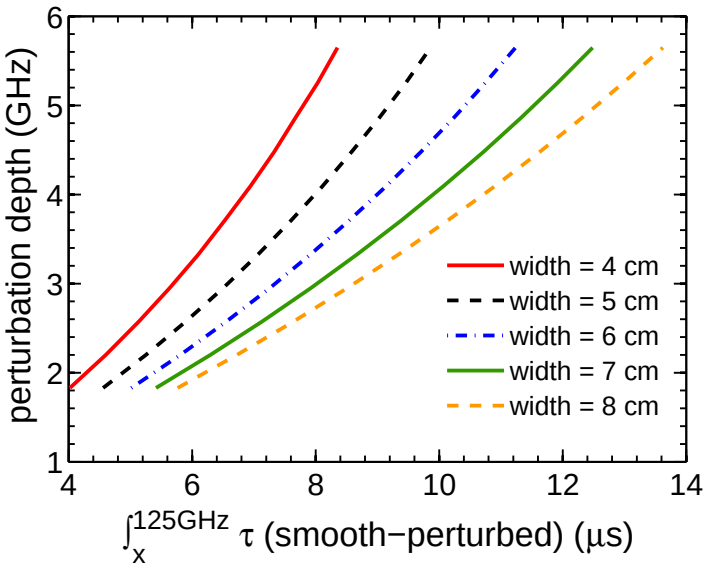

Figure 24: Relations of hole depth to the integral of the time-of-flight difference between perturbed and unperturbed cases. The integral in computed from the frequency where the signal crosses the unperturbed case until 20 GHz above the time of flight jump (in this case, 125 GHz).

These relations can be precisely fitted with polynomials of order two, with the parameters of the polynomials varying with the perturbation width. These relations are enough to reconstruct the perturbation for $sine^2$ shaped valleys.

9 Multiple perturbations

This section explores cases with multiple perturbations. More specifically, a bump followed by a valley. To start with simplified cases, the shapes are all assumed as $sine^2$ again, and the width of the bump is the same as the valley. Just as before, the perturbations are added on a fixed linear f_R profile. Instead of seeking inverting relations directly, the perturbations are added on the same profile but with varying widths. At each width value, the bump part is kept constant and the valley depth varies. The objective is to observe how each perturbation influences the time-of-flight signal in the cases where the vertical distribution of them shifts. Perturbations with two width examples are given in Figs. 25 and 26. In both cases, the middle depth of the valley (green curve) has the same amplitude as the bump. This gives the same area in f_R space for both the unperturbed and perturbed cases, meaning a null radially averaged perturbation.

The two examples in Figs. 25 and 26 were chosen as such because they show an uneven vertical distribution of the perturbation. On average, the bump lies on higher f_R values than the valleys. It is the exact opposite for a wide perturbation as in the examples in Fig. 26. This uneven vertical distribution is very significant for the time of flight signal after the perturbation. It comes from the same reasoning as the importance of the perturbation kurtosis in Sec. 7.2. If the bump and the valley are evenly distributed vertically in f_R, the time-of-flight signal after the jump quickly converges to the unperturbed solution if the bump height equals the valley depth. It is not the case for the examples in Fig. 25 and Fig. 26. The simulated time-of-flight signals, from the maximum of the IQ spectrogram, are found in Figs. 27 and 28.

The uneven vertical distribution of the perturbations in Figs. 25 and 26 are very evident from their respective time-of-flight signals in Figs. 27 and 28. In Fig. 27, there is always an excess in time-of-flight even when the valley is smaller than the bump. The fact that the bump is higher

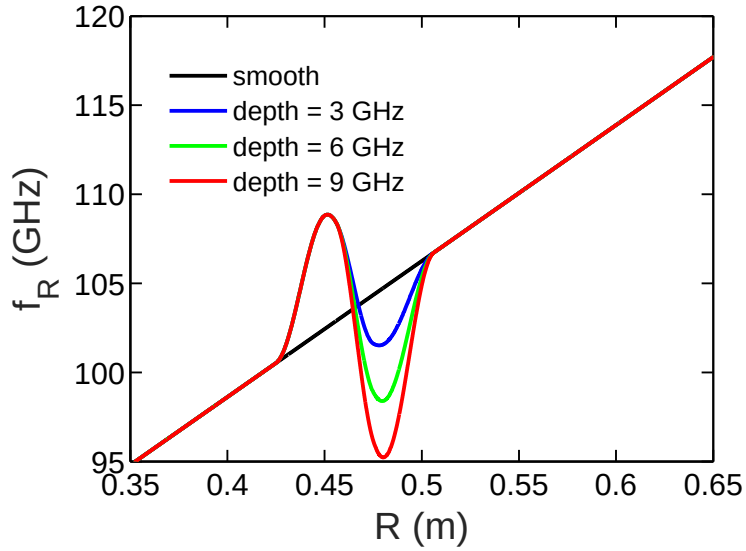

Figure 25: 9 cm long bump-valley perturbations added on a linear f_R profile. The valley has a varying depth while the bump is kept with a constant height of 6 GHz.

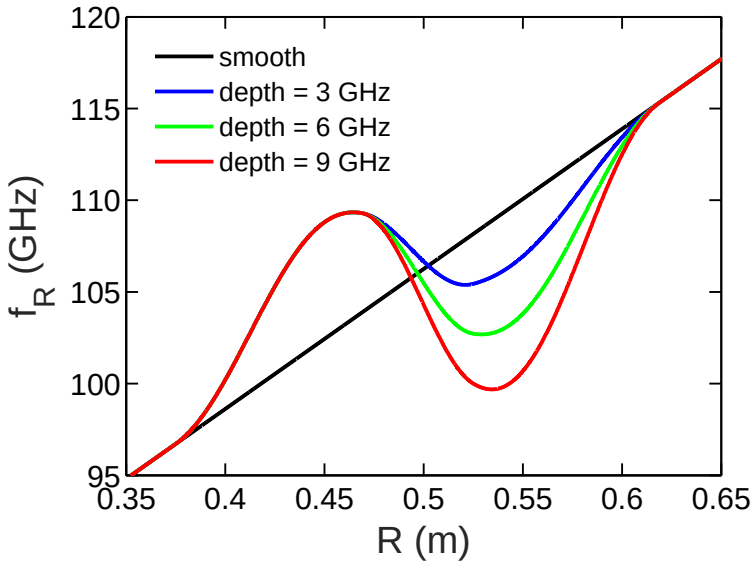

Figure 26: 25 cm long bump-valley perturbations added on a linear f_R profile. The valley has a varying depth while the bump is kept with a constant height of 6 GHz.

in f_R than the valley makes it contribute much more to the time-of-flight signal in the higher frequencies. Exactly the contrary, if the perturbation is wider and the valley is much higher in f_R than the bump, it contributes more to the time-of-flight of the higher frequencies. Fig. 28 shows how the excess in time-of-flight after the perturbation is always negative even when the valley is smaller than the bump. The reconstruction of such type of perturbations can still be done just like the $sine^2$ valleys in Sec. 8, but in addition the distribution in f_R along the perturbation has to be taken into account. This more sophisticated inversion method is currently under development.

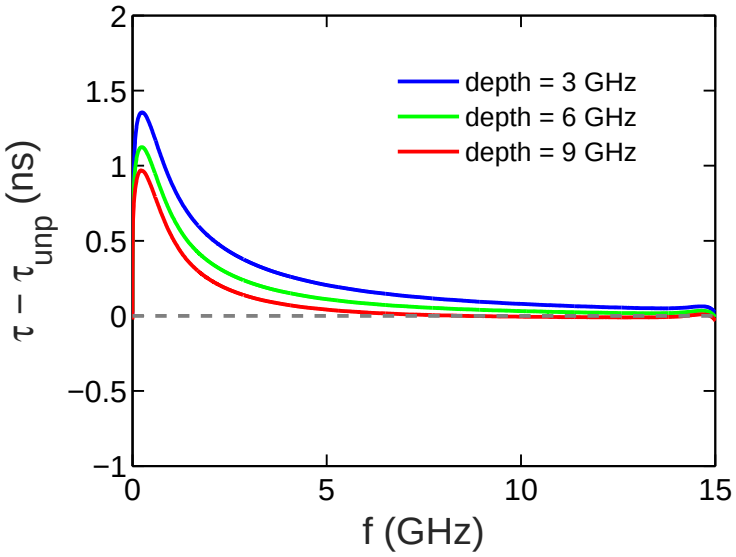

Figure 27: The maximum of the IQ spectrogram time-of-flight signal when simulating the sweep on the profiles presented in Fig. 25.

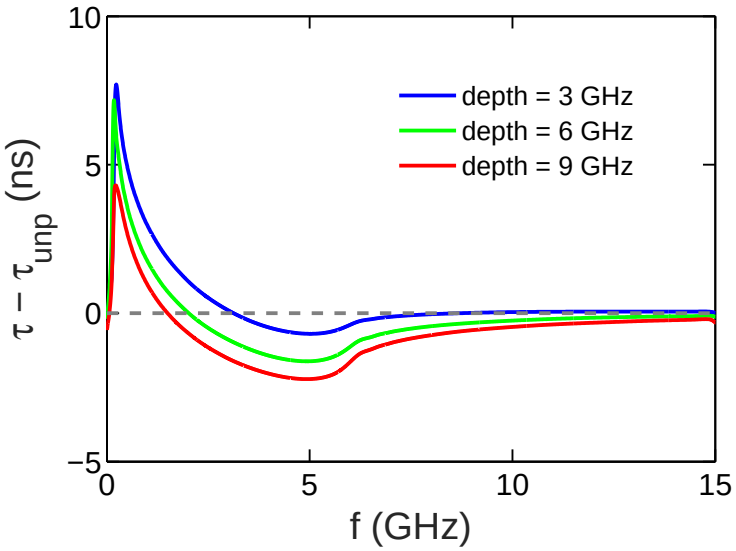

Figure 28: The maximum of the IQ spectrogram time-of-flight signal when simulating the sweep on the profiles presented in Fig. 26.

10 Conclusions and Future prospects

In the WKB framework, it was proven that there is information on the time-of-flight signal that relates to the size of the blind areas. In that case, the amplitude of the time-of-flight jump was used as a scaling parameter. When simulating the reflectometer signal with a 1D wave equation solver code, many full wave effects were added on the time-of-flight. These effects appeared mainly in the vicinity of the time-of-flight jump, making the jump amplitude an unreliable scaling parameter. The tunnelling effect, frequency mixing (or interferences) and resonances, are all time dependant effects that are affected by the reflectometer sweeping rate. In this contribution, the sweeping rate was

fixed just under the maximum sweeping rate used by the Tore Supra system, 20 GHz/μs. At this sweeping rate, the full-wave effects were restricted to less than 1 GHz before and after the time-of-flight jump. Beyond this band, the signals are compatible with the WKB approximation and have intuitive and reliable scaling features to the perturbation size. One possible implementation was the integral of the signal after crossing the unperturbed solution until converging to the unperturbed solution, like shown in Fig. 23. The relations acquired from this methodology are bound to $sine^2$ valleys. The adaptation to varying ∇f_R and to having multiple perturbations, as the first example of bump-valleys in Sec. 9, are currently being investigated.

The reconstructions techniques discussed here were based on a wide band after perturbations with a $sine^2$ shape. This region is dominated by WKB relevant signals and this approximation will be used to develop this approach further. On the other hand, the full-wave features can provide information regarding the perturbation shape. Although not discussed in this instance, these features will be investigated. However, the small amplitude and narrow band of the full-wave features can be easily masked by a high level of noise in the data.

Even though the main physical characteristics of the blind regions have been well described by the 1D simulations present in this contribution, 2D simulations are necessary for more realistic scalings. Eventually, 3D simulations should also be employed in the long term to verify any 3D effects. After all, the probing beam area and shape, plus the shape of the perturbations make in conjunction a system too complex to be simply described in 1 or 2 dimensions.

References

[1] S. Heuraux, S. Hacquin, F. da Silva, F. Clairet, R. Sabot, and G. Leclert. *Rev. Sci. Instrum.*, 74(1501), 2003.

[2] T. Gerbaud, F. Clairet, R. Sabot, A. Sirinelli, H. Heuraux, G. Leclert, and L. Vermare. *Rev. Sci. Instrum.*, 77(10E928), 2006.

[3] C. Fanack, I. Boucher, F. Clairet, S. Heuraux, G. Leclert, and X. L. Zou. *Plasma Phys. Control. Fusion*, 38(1915-1930), 1996.

[4] H. Bottollier-Curtet and G. Ichtchenko. *Rev. Sci. Instrum.*, 58(4), 1987.

[5] R. B. Morales, S. Hacquin, S. Heuraux, and R. Sabot. *Rev. Sci. Instrum.*, 88(043503), 2017.

[6] F. Clairet, R. Sabot, Ch. Bottereau, J. M. Chareau, and M. Paume. *Rev. Sci. Instrum.*, 72(1), 2001.

[7] K. G. Budden. Cambridge University Press, UK, 1966.

[8] E. Z. Gusakov, S. Heuraux, and A. Yu. Popov. *Plasma Phys. Control. Fusion*, 51(065018), 2009.

[9] F. Clairet, B. Ricaud, F. Briolle, S. Heuraux, and C. Bottereau. *Rev. Sci. Instrum.*, 82(083502), 2011.